a necessary consequence of Titan's widely varying seasonal insolation, will affect the magnitude of the surface sensible heat flux and change temperatures in the lower troposphere. If the lower tropospheric lapse rate is close to the boundary between stability and instability, as has been measured on Titan[13,15,16], a small additional heat flux can drive the creation of a thermally convective layer, the height of which will depend on the magnitude of the additional heat input and therefore on the surface temperature. Assuming the conditions least favourable to convection that have been inferred from Voyager measurements[13], even a surface temperature rise of only 1 K is sufficient to cause a convective layer 7 km in height. If this convective layer reaches the point at which methane saturates, the height of which is highly dependent on the methane humidity but is estimated to be around 4 km in typical models[6,12,15,16], methane condensation will render the air buoyant and drive clouds to the levels at about 15 km observed[17]. In regions with lower surface temperatures, the convective layer will be smaller or even non-existent, and condensation will not occur.

At the time of our observations, Titan was approaching southern summer solstice, and, owing to Titan's obliquity of 27°, the polar regions were in continuous sunlight and receiving more daily averaged insolation than any other spot on the satellite (and 50% more daily averaged insolation than the equator at equinox). We suggest that this insolation leads to a maximum surface temperature in these polar regions which drives a convective layer large enough to cause methane condensation and the ensuing moist convection. This hypothesis predicts that the location of these convective clouds will follow the location of maximum insolation (with some lag owing to the thermal inertia of the surface). □

Received 31 July; accepted 19 November 2002; doi:10.1038/nature01302.

1. Smith, P. H. *et al.* Titan's surface, revealed by HST imaging. *Icarus* **119,** 336–349 (1996).
2. Combes, M. *et al.* Spatially resolved images of Titan by means of adaptive optics. *Icarus* **129,** 482–497 (1997).
3. Gibbard, S. G. *et al.* Titan: High-resolution speckle images from the Keck telescope. *Icarus* **139,** 189–201 (1999).
4. Cousteins, A. *et al.* Images of Titan at 1.3 and 1.6 μm with adaptive optics at the CFHT. *Icarus* **154,** 501–515 (2001).
5. Griffith, C. A., Owen, T., Miller, G. A. & Geballe, T. Transient clouds in Titan's lower atmosphere. *Nature* **395,** 575–578 (1998).
6. Griffith, C. A., Hall, J. L. & Geballe, T. R. Detection of daily clouds on Titan. *Science* **290,** 509–512 (2000).
7. Wizinowich, P. *et al.* Performance of the W.M. Keck Observatory natural guide star adaptive optics facility: the first year at the telescope. *Proc. SPIE* **4007,** 2–13 (2000).
8. Bouchez, A. H., Brown, M. E., Griffith, C. A. & Dekany, R. G. Spatially resolved spectroscopy of Titan's surface and atmosphere. *Bull. Am. Astron. Soc.* **32,** 1702 (2000).
9. Lorenz, R. D., Young, E. F. & Lemmon, M. T. Titan's smile and collar: HST observations of seasonal change 1994-2000. *Geophys. Res. Lett.* **28,** 4453–4456 (2001).
10. Griffith, C. A., Hall, J. L., Young, E., Cook, J. & Rannou, P. Imaging temporal changes on Titan. *Icarus* (in the press).
11. Bouchez, A. H., Brown, M. E., Neyman, C. R., Troy, M. & Dekany, R. G. Ground-based visible adaptive optics observations of Titan's atmosphere and surface. *Icarus* (submitted).
12. Hunten, D. M. *et al. Saturn* (eds Gehrels, T. & Matthews, M. S.) 671–759 (Univ. Arizona Press, Tucson, 1984).
13. McKay, C. P., Martin, S. C., Griffith, C. A. & Keller, R. M. Temperature lapse rate and methane in Titan's troposphere. *Icarus* **129,** 498–505 (1997).
14. Tokano, T., Neubauer, F. M., Laube, M. & McKay, C. P. Three-dimensional modeling of the tropospheric methane cycle on Titan. *Icarus* **153,** 130–147 (2001).
15. Lindal, G. F. *et al.* The atmosphere of Titan: An analysis of the Voyager 1 radio-occultation measurements. *Icarus* **53,** 348–363 (1983).
16. Lellouch, E. *et al.* Titan's atmosphere and hypothesized ocean: A reanalysis of Voyager 1 radio-occultation and IRIS 7.7-μm data. *Icarus* **79,** 328–349 (1989).
17. Awal, M. & Lunine, J. I. Moist convective clouds in Titan's atmosphere. *Geophys. Res. Lett.* **21,** 2491–2494 (1994).
18. McLean, I. S. *et al.* The design and development of NIRSPEC: a near-infrared echelle spectrograph for the Keck II telescope. *Proc. SPIE* **3354,** 566–578 (1998).

Acknowledgements We thank E.J. Moyer and M.I. Richardson for conversations, D. Le Mignant, R. Campbell, M. Konacki and J. Eisner for acquiring the NIRC2 data, and S. Hörst for many nights of monitoring Titan in the cold. This work was supported by a grant from the NSF Planetary Astronomy programme.

Competing interests statement The authors declare that they have no competing financial interests.

Correspondence and requests for materials should be addressed to M.E.B. (e-mail: mbrown@caltech.edu).

Charge-ordered ferromagnetic phase in $La_{0.5}Ca_{0.5}MnO_3$

James C. Loudon, Neil D. Mathur & Paul A. Midgley

Department of Materials Science and Metallurgy, University of Cambridge, Pembroke Street, Cambridge CB2 3QZ, UK

Mixed-valent manganites are noted for their unusual magnetic, electronic and structural phase transitions. For example, the $La_{1-x}Ca_xMnO_3$ phase diagram[1] shows that below transition temperatures in the range 100–260 K, compounds with $0.2 < x < 0.5$ are ferromagnetic and metallic, whereas those with $0.5 < x < 0.9$ are antiferromagnetic and charge ordered. In a narrow region around $x = 0.5$, these totally dissimilar ground states are thought to coexist[2,3]. It has been shown[4] that charge order and charge disorder can coexist in the related compound, $La_{0.25}Pr_{0.375}Ca_{0.375}MnO_3$. Here we present electron microscopy data for $La_{0.5}Ca_{0.5}MnO_3$ that shed light on the distribution of these coexisting phases, and uncover an additional, unexpected phase. Using electron holography and Fresnel imaging, we find micrometre-sized ferromagnetic regions spanning several grains coexisting with similar-sized regions with no local magnetization. Holography shows that the ferromagnetic regions have a local magnetization of 3.4 ± 0.2 Bohr magnetons per Mn atom (the spin-aligned value is 3.5 μ_B per Mn). We use electron diffraction and dark-field imaging to show that charge order exists in regions with no net magnetization and, surprisingly, can also occur in ferromagnetic regions.

Figure 1 shows the temperature dependence of the magnetization for three different compositions of polycrystalline $La_{1-x}Ca_xMnO_3$ with a grain size of 5 μm (produced by Praxair, Woodinville, Washington, USA). These measurements were made in a field of 1 T with a vibrating sample magnetometer. The $x = 0.3$ compound (Fig. 1a) shows a standard paramagnetic-to-ferromagnetic phase transition at 256 K, and approaches the theoretical saturation moment of 3.7 μ_B per Mn (derived from the filling of the Mn *d* levels) at low temperatures (down to 10 K) as expected. The magnetization of the $x = 0.66$ compound (Fig. 1c) shows a paramagnetic-to-antiferromagnetic phase transition at 250 K. The $x = 0.5$ sample (from which the electron microscopy data is taken) appears to show both a paramagnetic-to-ferromagnetic transition at 233 K, and then an antiferromagnetic transition at 120 K measured on the cooling curve and 175 K on the warming curve (Fig. 1b). The large thermal hysteresis has been reported by other authors[1,5], and may be an indication that charge ordering is a 'nucleation and growth' process. Below the Néel temperature, the magnetization is still higher than at room temperature, and there are two possible causes of this effect: spin canting[6,7], or an inhomogeneous mixture of ferromagnetic and antiferromagnetic regions[2,4] within the same sample. We show here that the latter is the correct explanation.

According to the conventional models[8–10] for the low-temperature phase transitions in manganites, the antiferromagnetic phase is associated with a spontaneous ordering of Mn^{3+} and Mn^{4+} ions. If the room-temperature cell is indexed[11] as orthorhombic *Pnma* ($a = 5.42$ Å, $b = 7.65$ Å, $c = 5.44$ Å), the lattice distortion caused by this charge ordering gives rise to extra reflections at positions $(h + q, k, l)$ at low temperatures[12] in a diffraction pattern where q is the wavevector of the modulation. The wavevector has been seen to vary with both composition and temperature[13], but here we consider only the commensurate phase $q = 1/2$. If an objective aperture is placed over one of these reflections, parts of the sample that charge order appear bright in an image.

 © 2002 Nature Publishing Group

The $La_{0.5}Ca_{0.5}MnO_3$ sample was prepared for transmission electron microscopy by conventional mechanical polishing and argon-ion thinning at liquid-nitrogen temperatures. Large-area ($10 \times 10\,\mu m$) energy-dispersive X-ray analysis using a scanning electron microscope showed that the La/Ca ratio was constant to within the error of the measurements ($\delta x = \pm 2\%$). Transmission electron microscopy was undertaken using a 300-kV Philips CM300 microscope equipped with a field-emission gun to provide a coherent source of electrons, a biprism used for holography and a 'Lorentz' lens (a strong objective mini lens), which allows the magnetic structure of a specimen to be observed in near-zero (less than 0.02 T) magnetic field. A liquid-nitrogen specimen stage was used to cool the samples to 90 K.

We used two methods to image the magnetic structure of the material: Fresnel imaging and electron holography. In the Fresnel method[14], the sample is imaged out of focus with a coherent beam of electrons. Lorentz forces in the sample cause magnetic domain walls to appear[15] as bright interference fringes where the electrons converge, and as dark regions where the electrons diverge. In electron holography[16], an electron biprism (a positively charged wire) is inserted into the column of the microscope, and used to interfere a reference wave passing through vacuum with one passing through the sample. A digital reconstruction allows both the amplitude and phase of the exit wave-function to be determined directly.

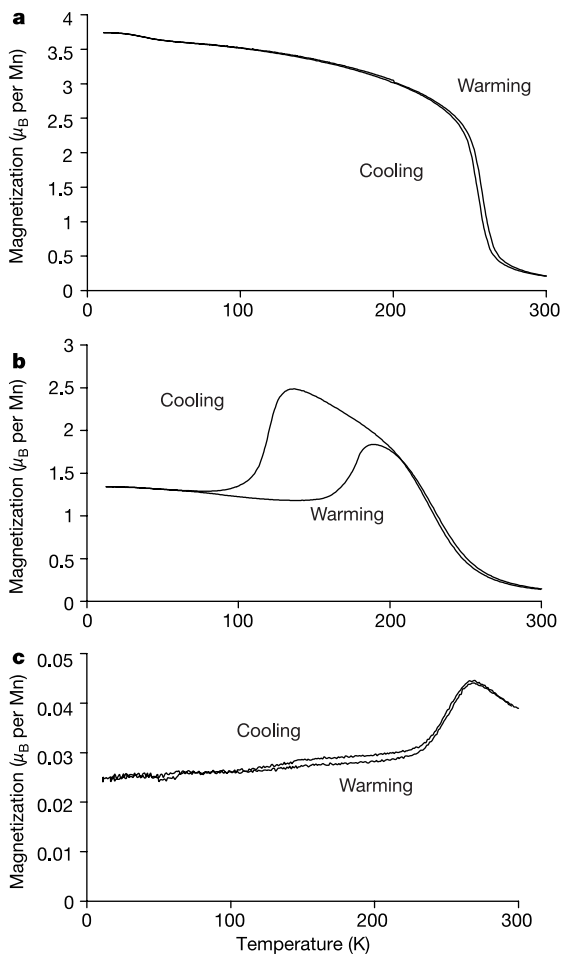

Figure 1 Curves of magnetization against temperature for various compositions of polycrystalline $La_{1-x}Ca_xMnO_3$ under an applied field of 1 T. **a**, $x = 0.3$ shows a conventional paramagnetic-to-ferromagnetic phase transition (with a Curie temperature of 256 K measured at the inflexion point), and approaches the saturation moment of 3.7 μ_B per Mn. The small hysteresis is almost certainly due to thermal inertia in the cryostat. **b**, $x = 0.5$ appears to show two transitions as the temperature is lowered: first, a paramagnetic-to-ferromagnetic transition at 233 K, and second, an antiferromagnetic transition at 120 K measured on the cooling curve and 175 K on the warming curve. **c**, $x = 0.66$ shows a paramagnetic-to-antiferromagnetic transition at 250 K.

Taking coordinates x and y normal to the beam direction z, the phase change on passing through the specimen is given by[16]

$$\phi(x,y) = C_E \int V_0(x,y,z)\mathrm{d}z - \frac{2\pi e}{h}\iint \mathbf{B}_\perp(x,y,z)\cdot\mathbf{dS} \qquad (1)$$

where $C_E = \frac{2\pi e}{\lambda}\left(\frac{eV+mc^2}{eV(eV+2mc^2)}\right) = 6.523\times10^6\,\mathrm{m^{-1}\,V^{-1}}$, e is the electron charge, m is the electron rest mass, V is the acceleration voltage (300 kV), c is the speed of light, λ is the wavelength of an electron (0.0197 Å at 300 kV), V_0 (x, y, z) is the mean inner potential, $\mathbf{B}_\perp(x,y,z)$ is the component of magnetic flux density normal to the electron beam, and **dS** is an element of vector area normal to the beam direction. This formula holds true provided that the specimen is not diffracting strongly. This is ensured by tilting away from any major zone axes.

By comparing holograms taken at room temperature (above the Curie temperature, T_C) with those taken at 90 K (below T_C), we can rearrange equation (1) to give a measure of the absolute value of the magnetization in a way that does not depend on the unknown thickness of the sample:

$$\begin{aligned}\mu_0\mathbf{M}_\perp(x,y) &= \mathbf{B}_\perp(x,y)\\ &= -\frac{h}{2\pi e}C_E V_0 \frac{1}{\phi_{T>T_C}(x,y)}\\ &\times \begin{pmatrix}\partial/\partial y\\ -\partial/\partial x\end{pmatrix}\left\{\phi_{T<T_C}(x,y) - \phi_{T>T_C}(x,y)\right\}\end{aligned} \qquad (2)$$

This formula assumes that: (1) V_0 is constant throughout the sample and has the value of 23.73 V calculated from electron scattering factors[17], (2) $\mathbf{B}_\perp(x, y)$ is constant throughout the thickness of the sample, and (3) the stray field is negligible in comparison with the flux density within the sample.

In Fig. 2 we show ferromagnetism and charge order coexisting. The field of view of a hologram is limited by the size of the interference region created by the biprism, and so we present Fig. 2a as a montage of regions investigated by holography (colour) overlaid on a Fresnel image. This image was taken using the Lorentz lens to focus the electrons. Typically, this lens places the specimen in a vertical magnetic field of less than 0.02 T. (Another Fresnel image showing domain walls in grain 2 is presented in Supplementary Fig. I). The Fresnel image shows long straight black and white lines in the lower left-hand corner. These are magnetic domain walls, which match the coloured domains derived from holography. (The black curves at the top right are bend contours.) Three grains are present in Fig. 2a, labelled 1, 2 and 3. In grain 1, the orthorhombic **b** axis lies approximately in the plane and 180° domains dominate, whereas in grain 2, the **b** axis lies approximately normal to the film and there is a mixture of 90° and 180° domains. This change in magnetic behaviour probably arises because of the change in the orientation of the unit cell and the shape anisotropy caused by the thin specimen[18].

The magnetization measured over 100×100 nm squares at several positions in several domains in grains 1 and 2 was 3.4 μ_B per Mn on average, with a standard deviation of 0.5 μ_B per Mn. If it is assumed that this variability comes only from random errors, we can give the average local magnetization as $3.4 \pm 0.2\,\mu_B$ per Mn. The holograms showed that the stray field in the vacuum near the specimen edge was approximately 5% of the flux density in the sample, so the stray field may be safely neglected. The mean inner potential V_0 was derived from electron scattering factors, assuming that all the atoms are neutral and no bonding takes place. This assumption is likely to overestimate the magnetization, possibly by

 © 2002 Nature Publishing Group

as much as 10%. In comparing this magnetization with the saturation moment, we assume that the magnetization lies in the plane of the specimen as would be expected by considering the shape anisotropy. The magnetization of $3.4 \pm 0.2\,\mu_B$ per Mn measured here agrees well with the value of $3.5\,\mu_B$ per Mn that would be expected if the sample were fully ferromagnetic, and is significantly larger than the bulk value of $1.25\,\mu_B$ per Mn measured by magnetometry.

Holography showed that grain 3 had no net magnetization, as did several other grains in other regions of the specimen. Figure 2e shows a diffraction pattern taken from the circled region in grain 3 showing charge ordering. This is the expected charge-ordered, non-ferromagnetic phase. We conclude that at 90 K, the sample is composed of an inhomogeneous mixture of ferromagnetic regions and regions with no net magnetization. Given that the bulk magnetization at this temperature is $1.25\,\mu_B$ per Mn (compared with the theoretical value of $3.5\,\mu_B$ per Mn), around 36% of the total sample is ferromagnetic.

Figure 2b shows a dark-field image from grain 2 taken using the (1/2, 0, 2) (charge-ordered) reflection, and Fig. 2c shows the associated diffraction pattern taken from the region circled in grain 2, showing charge-ordered reflections at positions $(h + 1/2, k, l)$. These images were taken with the Lorentz lens turned off and the electrons focused with the main objective lens, which places the sample in a vertical magnetic field of around 2 T. This will tend to cause the magnetization to rotate towards the optic axis, and possibly cause the charge-ordered regions to shrink. Despite this, both the diffraction pattern and the dark-field image show charge order present in the region of the sample where holography revealed ferromagnetic domains. The simplest explanation for the dark-field contrast seen in grain 2 (Fig. 2b) is that the bright regions are charge ordered and ferromagnetic, and the dark regions are ferromagnetic and charge disordered.

We now consider the possibility that the ferromagnetic charge-ordered phase is in fact made of charge-ordered antiferromagnetic regions coexisting with ferromagnetic metallic regions on a very small scale. The spatial resolution of the dark-field image is determined primarily by the size of the objective aperture and the specimen drift rate, and is about 2 nm in this case. The spatial resolution of the holograms is limited by the size of the window used in the Fourier filtering process as part of the reconstruction process and is about 20 nm; the system can therefore resolve the magnetization and its distribution in any region several times larger than this. The large bright patch in the dark-field image (Fig. 2b), which overlaps the magnetic region in Fig. 2a, is about 100 nm in size. Thus if a small-scale segregation takes place, the coexisting phases must be less than 2 nm (about four unit cells parallel to the **a** axis) in size; this must be regarded as mesoscopic texture rather than two thermodynamically stable phases as argued in ref. 3. Furthermore, if this were the case, we would expect the magnetization in the overlapping region to be approximately halved. In fact, the magnetization in this region is $3.5 \pm 0.2\,\mu_B$ per Mn, in excellent agreement with the spin-

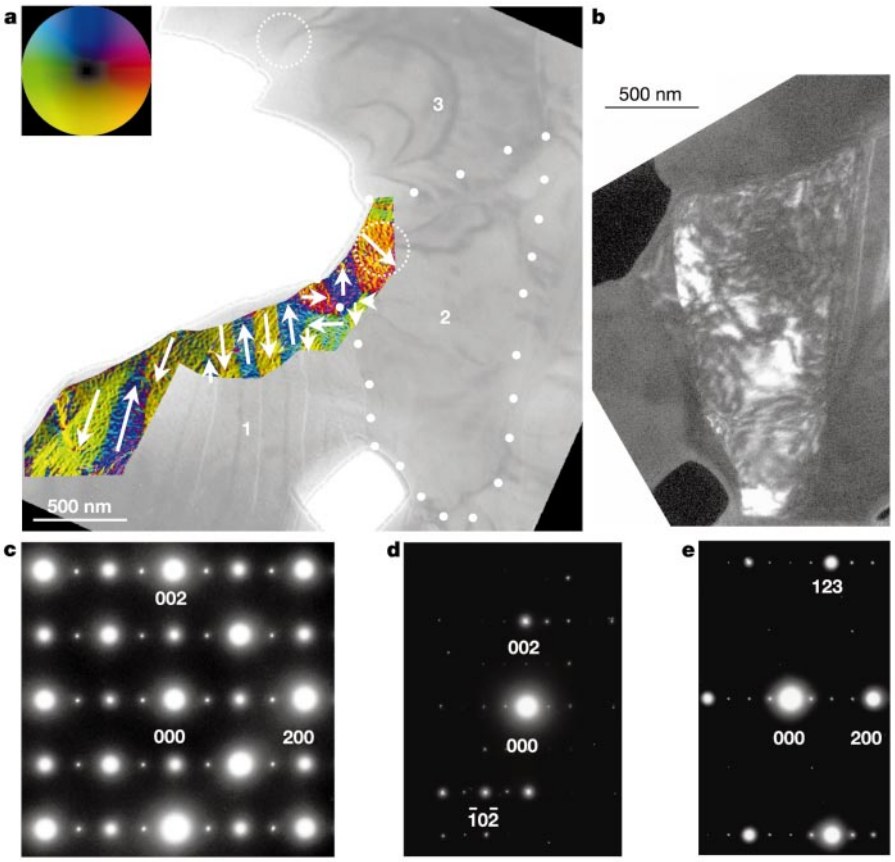

Figure 2 Coexistence of ferromagnetism and charge order. Three grains (labelled 1, 2 and 3) are present in the image. The grain boundary is indicated by the white dots. **a**, A colour image of the magnetic structure derived from available holography data overlaid on a Fresnel image. The colour wheel indicates the direction of the local magnetization (marked with arrows). The apparent texture within each domain is likely to be an artefact of the Fourier filtering process used to reconstruct the phase of the exit wavefunction. **b**, A dark-field image on the same scale from grain 2, taken using the (1/2, 0, 2) charge-ordered reflection. **c**, A diffraction pattern taken from the circled region in 2 looking down the [010] axis with charge-ordered reflections at $(h + 1/2, k, l)$. **d**, A diffraction pattern from the same region as **c** tilted away from the [010] zone axis by a few degrees. The charge-ordered reflections persist, but reflections of type (00*l*) (for *l* odd) are now absent as they are kinematically forbidden by the *Pnma* space group. **e**, A diffraction pattern from the circled region in grain 3 looking down the $[03\bar{2}]$ zone axis. Charge-ordered reflections can be seen at $(h + 1/2, k, l)$. Holography showed that this region had no net magnetization. The very weak reflections between the main rows are from a twin variant of this axis, the [214] zone axis.

© 2002 Nature Publishing Group

aligned value of 3.5 μ_B per Mn. It is also possible that this region may be a ferromagnetic phase on top of a separate non-ferromagnetic, charge-ordered phase. If so, the charge-ordered phase would have to be less than 2 nm (about two unit cells parallel to the **b** axis) thick to produce a magnetization within the error limits quoted. Such a thin region is unlikely, because the region of interest is very bright in the dark-field image (Fig. 2b), indicating that charge order is well established here. We have also taken a number of Fresnel images and diffraction patterns from other areas of the sample, and have seen magnetic domain walls and charge ordering in the same region (Supplementary Fig. II), which is further evidence for this unexpected phase.

In tilting the sample, we found that charge-ordered reflections perpendicular to a systematic row were far stronger for those parallel to the systematic row. Figure 2d shows a systematic row from the same region as Fig. 2c with strong charge-ordered reflections perpendicular to the row. This is strong evidence that charge order is predominantly a transverse modulation of the atoms, as discussed in ref. 11 based on evidence from neutron powder diffraction.

Using electron microscopy, we have shown that at 90 K, $La_{0.5}Ca_{0.5}MnO_3$ forms an inhomogeneous mixture of ferromagnetic and zero-moment (presumably antiferromagnetic[1]) regions. Each region extends for several micrometres, and can span several crystallographic grains. Our results suggest that charge order occurs not only in regions with no net magnetization, but can also occur in ferromagnetic regions. Very recently, evidence has been published[19] that is consistent with the possibility of a similar coexistence in $La_{0.25}Pr_{0.375}Ca_{0.375}MnO_3$. This charge-ordered, ferromagnetic phase is not predicted by conventional models[8–10], but unexpected phases such as this can arise from a simple hamiltonian[20].

We suggest that the bandgap that opens up below the charge-ordering transition temperature can be small enough that the valence electrons still have enough mobility to promote ferromagnetism via double exchange, and yet large enough to produce a charge density wave. This seems reasonable, as ferromagnetic coupling in the manganites should only require nearest-neighbour hopping. Furthermore, some degree of charge ordering may even be possible deep within the ferromagnetic regime, as diffuse charge-ordered reflections have been observed[21] in $La_{2/3}Ca_{1/3}MnO_3$. We further suggest that the bandgap is locally modified by strain within each grain, and that this results in the rich variety of phases that can coexist in the manganites. This may also explain the strong dependence of $La_{0.5}Ca_{0.5}MnO_3$ properties on grain size[5]. Therefore manganite phase diagrams based on composition alone paint an inadequate picture of manganite physics, and miss the richness and complexity that we have demonstrated here. □

Received 18 June; accepted 14 November 2002; doi:10.1038/nature01299.

1. Cheong, S.-W. & Hwang, H. Y. *Colossal Magnetoresistive Oxides* Monographs in Condensed Matter Science, Ch. 7 (ed. Tokura, Y.) (Gordon & Breach, Reading, UK, 2000).
2. Moreo, A., Yunoki, S. & Dagotto, E. Phase separation scenario for manganese oxides and related materials. *Science* **283,** 2034–2040 (1999).
3. Mathur, N. D. & Littlewood, P. B. The self-organised phases of manganites. *Solid State Commun.* **119,** 271–280 (2001).
4. Uehara, M., Mori, S., Chen, C. H. & Cheong, S.-W. Percolative phase separation underlies colossal magnetoresistance in mixed valent manganites. *Nature* **399,** 560–563 (1999).
5. Levy, P. *et al.* Controlled phase separation in $La_{0.5}Ca_{0.5}MnO_3$. *Phys. Rev. B* **62,** 6437–6441 (2000).
6. Radaelli, P. G., Cox, D. E., Capogna, L., Cheong, S.-W. & Marezio, M. Wigner-crystal and bi-stripe models for the magnetic and crystallographic superstructures of $La_{0.333}Ca_{0.667}MnO_3$. *Phys. Rev. B* **59,** 14440–14450 (1999).
7. Roy, M., Mitchell, J. F., Ramirez, A. P. & Schiffer, P. Doping-induced transition from double exchange to charge order in $La_{1-x}Ca_xMnO_3$ near $x = 0.5$. *Phys. Rev. B* **58,** 5185–5188 (1998).
8. Goodenough, J. B. Theory of the role of covalence in the perovskite type manganites [La,M(II)]MnO_3. *Phys. Rev.* **100,** 564–573 (1955).
9. De Gennes, P.-G. Effects of double exchange in magnetic crystals. *Phys. Rev.* **118,** 141–154 (1960).
10. Zener, C. Interaction between the d shells in the transition metals. II. Ferromagnetic compounds of manganese with perovskite structure. *Phys. Rev.* **82,** 403–405 (1951).
11. Radaelli, P. G., Cox, D., Marezio, M. & Cheong, S.-W. Charge, orbital and magnetic ordering in $La_{0.5}Ca_{0.5}MnO_3$. *Phys. Rev B* **55,** 3015–3023 (1997).
12. Mori, S., Chen, C. H. & Cheong, S.-W. Pairing of charge-ordered stripes in (La,Ca)MnO_3. *Nature* **392,** 473–476 (1998).
13. Chen, C. H., Cheong, S.-W. & Hwang, H. Y. Charge-ordered stripes in $La_{1-x}Ca_xMnO_3$ with $x > 0.5$. *J. Appl. Phys.* **81,** 4326–4330 (1997).
14. Hirsh, P., Howie, A., Nicholson, R., Pashley, D. W. & Whelan, M. J. *Electron Microscopy of Thin Crystals*, 2nd edn (Krieger, Malabar, Florida, 1977).
15. Lloyd, S. J., Mathur, N. D., Loudon, J. C. & Midgley, P. A. Magnetic domain wall width in $La_{0.7}Ca_{0.3}MnO_3$ thin films using Fresnel imaging. *Phys. Rev. B* **64,** 172407 (2001).
16. Dunin-Borkowski, R. E., McCartney, M. R, Smith, D. J. & Parkin, S. S. P. Towards quantitative electron holography of magnetic thin films using in-situ magnetization reversal. *Ultramicroscopy* **74,** 61–73 (1998).
17. Rez, D., Rez, P. & Grant, I. Dirac-Fock calculations of x-ray scattering factors and contributions to the mean inner potential for electron scattering. *Acta Crystallogr. A* **50,** 481–497 (1994).
18. Suzuki, Y. *et al.* Magnetic anisotropy of doped manganite thin films and crystals. *J. Appl. Phys.* **83,** 7064–7066 (1998).
19. Mori, S., Asaka, T. & Matsui, Y. Observation of magnetic domain structure in phase-separated manganites by Lorentz electron microscopy. *J. Electron Microsc.* **51,** 225–229 (2002).
20. Yunoki, S., Hotta, T. & Dagotto, E. Ferromagnetic A-type, and charge-ordered CE-type states in doped manganites using Jahn-Teller phonons. *Phys. Rev. Lett.* **84,** 3714–3717 (2000).
21. Zuo, J. M. & Tao, J. Nanometer-sized regions of charge ordering and charge melting in $La_{2/3}Ca_{1/3}MnO_3$ revealed by electron microdiffraction. *Phys. Rev. B* **63,** 060407 (2001).

Supplementary Information accompanies the paper on *Nature*'s website (**http://www.nature.com/nature**).

Acknowledgements We thank R. Dunin-Borkowski for help with electron holography, D. Vowles for help in using the scanning electron microscope, A. Williams and J. P. Attfield for discussions, and A. J. Millis and P. B. Littlewood for information on the nature of charge order. This work was funded by the UK EPSRC and by the Royal Society.

Competing interests statement The authors declare that they have no competing financial interests.

Correspondence and requests for materials should be addressed to J.C.L. (e-mail: james.loudon@physics.org).

Electroluminescence from single monolayers of nanocrystals in molecular organic devices

Seth Coe*†, Wing-Keung Woo†‡, Moungi Bawendi‡ & Vladimir Bulović*

** Laboratory of Organic Optoelectronics, Department of Electrical Engineering and Computer Science,*
‡ Center for Materials Science and Engineering, Department of Chemistry, Massachusetts Institute of Technology, Cambridge, Massachusetts 02139, USA
† These authors contributed equally to this work

The integration of organic and inorganic materials at the nanometre scale into hybrid optoelectronic structures enables active devices[1–3] that combine the diversity of organic materials with the high-performance electronic and optical properties of inorganic nanocrystals[4]. The optimization of such hybrid devices ultimately depends upon the precise positioning of the functionally distinct materials. Previous studies[5,6] have already emphasized that this is a challenge, owing to the lack of well-developed nanometre-scale fabrication techniques. Here we demonstrate a hybrid light-emitting diode (LED) that combines the ease of processability of organic materials with the narrow-band, efficient luminescence of colloidal quantum dots[7] (QDs). To isolate the luminescence processes from charge conduction, we fabricate a quantum-dot LED (QD-LED) that contains only a single monolayer of QDs, sandwiched between two organic thin films. This is achieved by a method that uses material phase segregation between the QD aliphatic capping groups and the aromatic organic materials. In our devices, where QDs function exclusively as lumophores, we observe a 25-fold improvement in luminescence efficiency (1.6 cd A^{-1} at 2,000 cd m^{-2}) over the best previous QD-LED results[5]. The reproducibility and precision of our